Detailed Analysis of DC-Link Virtual Impedance-Based Suppression Method for Harmonics Interaction in High-Power PWM Current-Source Motor Drives

Ye Zhang, *Student Member, IEEE*, and Yun Wei Li, *Senior Member, IEEE*

***Abstract*—For high-power PWM current-source motor drive systems, due to the low converter switching frequency and the relative small dc choke for reduced cost/weight, the converters' switching harmonics may interact through dc link and produce interharmonics in the entire system. Such harmonics interaction phenomenon may give rise to the system resonance at certain motor speeds, which degrades the grid-side power quality and generates excessive torque ripples on the motor side. The resonance caused by the harmonics interaction in high-power PWM current-source motor drives is investigated in previous study. In addition, to actively suppress such resonance, the basic idea of a dc-link virtual impedance-based suppression method has also been proposed. This paper extends the previous study to thoroughly analyze the mechanism and realization of resonance suppression by the dc-link virtual impedance-based method. The in-depth analysis shows that the dc-link virtual impedance-based method successfully enables the active interharmonics compensation capability of high-power PWM current-source drives, which is not addressed in previous researches. Moreover, simulations and experiments demonstrate that, by following the selection of coefficient in the suppression method discussed in this paper, the dc-link virtual impedance-based method can effectively enhance the attenuation effect of dc link in high-power PWM current-source drive systems so as to suppress the resonance due to the harmonics interaction under all resonance conditions.**

***Index Terms*—Current-source drives, harmonics interaction, high-power converter, selective harmonic elimination (SHE), virtual impedance.**

I. Introduction

FOR high-power PWM current-source motor drives, the converter switching frequency is commonly confined to a few hundred Hertz to reduce the switching losses, and the dc choke is minimized to a reasonably low value (<0.8 p.u.) to reduce the size, weight, and cost [1], [2]. An example topology of PWM current-source motor drive systems is shown in Fig. 1. In such a high-power drive system, the selective harmonic elimination (SHE) scheme is commonly adopted, as it can mitigate the low-order harmonics generated by the PWM converters with a very low switching frequency. Nevertheless,

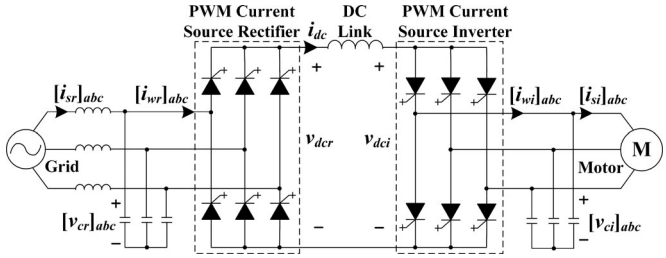

Fig. 1. Typical structure of PWM current-source drive systems.

with a small dc choke, the dc-link current harmonics (especially the lower-order harmonics) generated by the current-source rectifier (CSR) and the current-source inverter (CSI) cannot be attenuated sufficiently. The distorted dc-link current will introduce interharmonics in both the grid side and the motor side through the converters. The introduced ac-side interharmonics will further produce additional harmonics in dc link through the CSR and the CSI. As a result, the process of harmonics interaction between the CSR and the CSI through the dc link may introduce interharmonics at various frequencies. Since a three-phase capacitor is required to assist the commutation of switching devices in PWM current-source system as shown in Fig. 1, it forms a *LC* resonance in both the grid side and the motor side with grid-side line inductance and motor-side leakage inductance, respectively. When the motor operates at certain speeds, the frequencies of the introduced interharmonics can become close to the ac-side *LC* resonant frequency that gives rise to system resonance.

Regarding the harmonics interaction phenomenon in high-power PWM current-source drive systems, [3] provides a thorough investigation of its generation mechanism and excitation of system resonance. According to [3], when the harmonics interaction results in the system resonance, significant interharmonics will be introduced in grid-side line current, dc-link current, and motor-side stator current, which causes poor grid power quality, extra system losses, and cumulative damage or even immediate failure of mechanical system. Currently, the mostly used method of system resonance suppression is through passive damping, which involves additional costs and losses in system and may aggravate the size and weight of dc-link choke in high-power current-source drives. Therefore, to avoid the resonance excited by the harmonics interaction,

Manuscript received May 2, 2014; revised June 30, 2014; accepted September 26, 2014. Date of publication October 2, 2014; date of current version April 15, 2015. Recommended for publication by Associate Editor P. C.-K. Luk.

The authors are with the Department of Electrical and Computer Engineering, University of Alberta, Edmonton, AB T6G 2V4 Canada (e-mail: ye17@ualberta.ca; yunwei.li@ualberta.ca).

Color versions of one or more of the figures in this paper are available online at http://ieeexplore.ieee.org.

Digital Object Identifier 10.1109/TPEL.2014.2361435

active resonance suppression is expected for the high-power PWM current-source drive systems. It requires the commonly used SHE scheme in high-power PWM drives to have the active compensation capability of interharmonics. However, on the one hand, since the modulation index of SHE scheme is fixed in a fundamental cycle, the proposed active damping techniques through regulating the modulation index of space-vector-modulation (SVM)-based PWM converters [4]–[12] cannot be applied. On the other hand, the proposed methods with focus on the active compensation ability of SHE-modulated converters, the selective harmonics compensation PWM scheme [13], [14], can realize the steady-state compensation of the harmonics in the systems, but is unable to mitigate the interharmonics resulted from the harmonics interaction. To suppress the resonance caused by the harmonics interaction in high-power PWM current-source drive systems, the basic idea of a dc-link virtual impedance-based active suppression method is presented in [3]. The dc-link virtual impedance, if designed and realized properly, can compensate the system interharmonics through the SHE-modulated PWM current-source converters, so that the resonance excited by the harmonics interaction is effectively suppressed.

As the effectiveness of the virtual impedance highly dependent on the design and implementation techniques, this paper extends the previous study in [3] to thoroughly investigate the mechanism of the dc-link virtual impedance-based method to realize the interharmonics compensation capability of SHE-modulated PWM current-source converters, and achieve the active suppression of resonance caused by the harmonics interaction in high-power PWM current-source motor drive systems. Based on the investigation, the selection rule of the coefficient in the dc-link virtual impedance-based suppression method is discussed according to different resonance conditions. Extensive simulations and experiments are provided in this paper to demonstrate that the selection of coefficient guarantees effective resonance suppression under all motor speeds.

II. DC-Link Virtual Impedance-Based Resonance Suppression Method

As aforementioned, to actively suppress the resonance caused by the harmonics interaction in high-power PWM current-source drives, a dc-link virtual impedance-based method has been proposed in [3]. In this section, the idea of virtual impedance is briefly reviewed.

According to [3], the root cause of harmonics interaction in high-power PWM current-source drive systems is the weak attenuation effect of the small dc choke on current harmonics (especially lower-order harmonics). Therefore, if the dc-link impedance could be increased, the rectifier-side harmonics and the inverter-side harmonics will be decoupled so that the resonance will be prevented from being excited by the harmonics interaction. Furthermore, if the increase of dc-link impedance could be virtually realized through the feedback of dc-link current as illustrated in Fig. 2, the additional costs/losses and the aggravation of size/weight involved with the physical

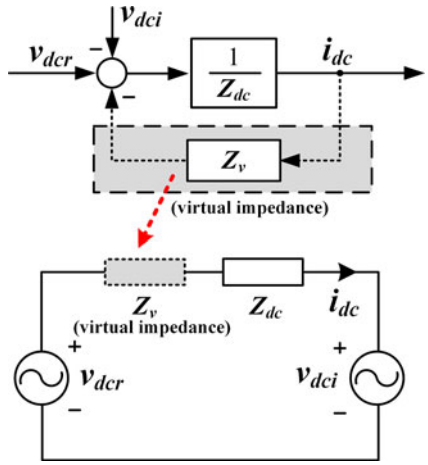

Fig. 2. Concept of virtual dc-link impedance.

increase of impedance can be avoided. In Fig. 2, v_{dcr}, v_{dci}, and $i_{\rm dc}$ are the rectifier-side dc-link voltage, inverter-side dc-link voltage, and dc-link current as shown in Fig. 1, and $Z_{\rm dc}$ is the real dc-link impedance.

Based on the virtual dc-link impedance concept, the dc-link virtual impedance-based resonance suppression method can be depicted as the dash block in a typical speed control scheme of PWM current-source drives shown in Fig. 3. In such a speed control system, the dc-link current is controlled through the CSR (by delay angle α control) and the CSI is maintained with a maximum modulation index (to minimize the dc-link current so as to reduce losses). The CSR is modulated with SHE scheme while the CSI adopts SHE at high motor speed and SVM at low motor speed [15]–[18]. To realize the virtual dc-link impedance concept, the dc-link current harmonics are fed back to the rectifier-side firing angle $\theta_{\rm rec}$, through a compensation signal $\theta_{\rm comp}$ shown in Fig. 3. The resonant filter in the feedback channel is required to filter out the dc component and the high-frequency noise harmonics in $i_{\rm dc}$ so as not to affect the original speed control scheme. To suppress the resonance excited by the harmonics interaction, the passband frequency of the resonant filter is selected at the frequency of the significant harmonics in dc-link current, which are caused by the harmonics interaction. Such frequencies can be accurately predicted by the resonance estimation method proposed during the investigation of the harmonics interaction in [3]. By doing so, the dc-link current harmonics due to the harmonics interaction can be attenuated, so that the harmonics interaction through the dc link in high-power PWM current-source drives can be suppressed. As a result, the resonance can be avoided being excited by the harmonics interaction.

With respect to the dc-link virtual impedance-based suppression method, only the basic idea is presented in [3]. To effectively apply this method, an in-depth analysis on the mechanism of active compensation based on the SHE-modulated PWM current-source converters and the realization of dc-link virtual impedance to suppress the resonance in high-power PWM current-source drives are important, and will be provided in the following two sections.

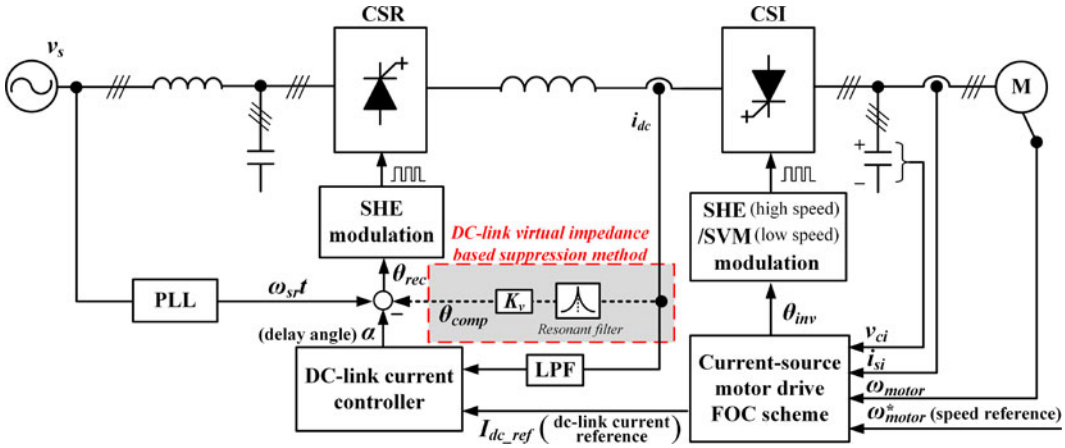

Fig. 3. Dc-link virtual impedance-based suppression method in typical speed control scheme of PWM current-source drives.

III. Enabled Interharmonics Compensation Capability of SHE-Modulated PWM Converters

As previously discussed, to realize the active resonance suppression based on the dc-link virtual impedance concept, the PWM converters need to be capable of actively compensating the dc-link current harmonics. With respect to the resonance caused by the harmonics interaction, the frequencies of the introduced dc-link current harmonics are commonly neither integer multiple of grid-side fundamental frequency nor motor-side fundamental frequency. Therefore, the SHE-modulated PWM converters in high-power PWM current-source drives are further required to have the interharmonics compensation capability. However, the previous researches related to the active compensation capability of the SHE-modulated PWM converters [13], [14] only focus on the compensation of the harmonics with integer multiple of ac-side fundamental frequency. In this section, the advantage of the dc-link virtual impedance-based method to enable the interharmonics compensation capability of SHE-modulated converters will be analyzed in detail. It also provides the fundamentals for the analysis of dc-link virtual impedance's realization discussed in next section.

In Fig. 3, the modulation functions of PWM CSR can be defined as S_{wra}, S_{wrb}, S_{wrc} for each phase

$$S_{wrk}=\begin{cases}1, & \text{the upper switch in phase } k \text{ is on}\\ -1, & \text{the lower switch in phase } k \text{ is on } (k=a,b,c)\\ 0, & \text{both switches in phase } k \text{ is on/off.}\end{cases} \tag{1}$$

Then, the phasor of modulation functions can be obtained as

$$\vec{S}_{wr}=\sum_h -jM_{srh}e^{j(h\theta_{\rm rec}+\varphi_{srh})} \quad (h=1,-5,7,-11,13,\ldots) \tag{2}$$

where M_{srh} and φ_{srh} are the magnitude and initial phase of hth-order harmonics in SHE PWM pattern, respectively, $\theta_{\rm rec}$ is the rectifier-side firing angle as mentioned previously. The positive h represents the positive sequence, and the negative h represents the negative sequence. When h is negative, $M_{srh}=-M_{sr(-h)}$ and $\varphi_{srh}=-\varphi_{sr(-h)}$.

Consider the fundamental component $\vec{S}_{wr1}$ $(h=1)$ in (2). Since M_{sr1} (also known as modulation index) is fixed around 1 and φ_{sr1} is designed to be 0 in SHE PWM pattern, we can obtain (3) as

$$\vec{S}_{wr1}=-je^{j(\theta_{\rm rec})}. \tag{3}$$

Before adopting the dc-link virtual impedance-based suppression method, we can obtain (4) according to Fig. 3

$$\theta_{\rm rec}=\omega_{sr}t-\alpha. \tag{4}$$

Substituting (4) into (3), (5) can be obtained as

$$\vec{S}_{wr1}=-je^{j(\omega_{sr}t-\alpha)} \tag{5}$$

where ω_{sr} is the grid-side fundamental frequency; α is the delay angle as mentioned previously. Note that the delay angle α, which is the phase angle of fundamental component in SHE PWM pattern, is used to control the dc-link current, and it will be constant at steady state.

After using the dc-link virtual impedance-based method, a compensation signal $\theta_{\rm comp}$ is introduced into $\theta_{\rm rec}$ as shown in Fig. 3. At steady state, it can be represented as an alternating signal $\theta_{\rm comp}=M_{\rm comp}\sin(\omega_{\rm comp}t+\varphi_{\rm comp})$, where $M_{\rm comp}$, $\omega_{\rm comp}$, and $\varphi_{\rm comp}$ are the magnitude, frequency, and initial phase, respectively. Then, we can obtain the new rectifier-side firing angle as

$$\begin{aligned}\theta'_{\rm rec} &= \omega_{sr}t-\alpha+\theta_{\rm comp}\\ &= \omega_{sr}t-\alpha+M_{\rm comp}\sin(\omega_{\rm comp}t+\varphi_{\rm comp}).\end{aligned} \tag{6}$$

Substituting (6) into (3), the new component generated by the fundamental SHE component $\vec{S}_{wr1}$ and the compensation signal $\theta_{\rm comp}$, defined as $\vec{S}^{\rm SHE_1}_{wr}$, can be obtained as shown in (7)

$$\vec{S}^{\rm SHE_1}_{wr}=-je^{j(\theta'_{\rm rec})}=-je^{j(\omega_{sr}t-\alpha+M_{\rm comp}\sin(\omega_{\rm comp}t+\varphi_{\rm comp}))}. \tag{7}$$

Taking Jacobi–Anger extension [19], (7) can be rewritten as

$$\vec{S}^{\rm SHE_1}_{wr} = -jJ_0(M_{comp})e^{j(\omega_{sr}t-\alpha)}$$

$$-j\sum_{k=1}^{\infty} J_k(M_{\text{comp}})e^{j((\omega_{sr}+k\omega_{\text{comp}})t-\alpha+k\varphi_{\text{comp}})}$$
$$-j\sum_{k=1}^{\infty} (-1)^k J_k(M_{\text{comp}})e^{j((\omega_{sr}-k\omega_{\text{comp}})t-\alpha-k\varphi_{\text{comp}})} \quad (8)$$

where $J(\cdot)$ is the Bessel function. According to Bessel function properties, when M_{comp} is small, three approximations can be achieved as $J_0(M_{\text{comp}}) \approx 1$, $J_1(M_{\text{comp}}) \approx 0.5M_{\text{comp}}$, and $J_2(M_{\text{comp}}) \approx 0 (k \geq 2)$. By utilizing these approximations, (9) can be obtained from (8) as

$$\vec{S}_{wr}^{\text{SHE}_1} \approx \vec{S}_{wr1}^{\text{SHE}_1} + \vec{S}_{wr\_Ls}^{\text{SHE}_1} + \vec{S}_{wr\_Rs}^{\text{SHE}_1},$$
$$\text{where} \begin{cases} \vec{S}_{wr1}^{\text{SHE}_1} = -je^{j(\omega_{sr}t-\alpha)} \\ \vec{S}_{wr\_Ls}^{\text{SHE}_1} \approx j0.5M_{\text{comp}}e^{j((\omega_{sr}-\omega_{\text{comp}})t-\alpha-\varphi_{\text{comp}})} \\ \vec{S}_{wr\_Rs}^{\text{SHE}_1} \approx -j0.5M_{\text{comp}}e^{j((\omega_{sr}+\omega_{\text{comp}})t-\alpha+\varphi_{\text{comp}})}. \end{cases} \quad (9)$$

It can be observed from (9) that, after adding the compensation signal θ_{comp}, two sideband harmonics, $\vec{S}_{wr\_Ls}^{\text{SHE}_1}$ (left side) and $\vec{S}_{wr\_Rs}^{\text{SHE}_1}$ (right side), are introduced around the new fundamental component $\vec{S}_{wr1}^{\text{SHE}_1}$. Their magnitude (0.5 M_{comp}), frequency ($\omega_{sr} \pm \omega_{\text{comp}}$), and phase angle ($-\alpha \pm \varphi_{\text{comp}}$) are not only all controllable through θ_{comp}, but also have a simple algebraic correspondence to the magnitude (M_{comp}), frequency (ω_{comp}), and phase angle (φ_{comp}) of θ_{comp}. It enables the real-time active compensation capability of the SHE-modulated PWM converters. In addition, since their frequencies can be arbitrarily adjusted by ω_{comp}, the SHE-modulated converters can be further adopted to compensate the interharmonics in the system. For example, according to Fig. 3, the two sideband harmonics introduced by θ_{comp} in rectifier-side PWM pattern can be combined with the grid-side voltage/current to compensate dc-link current harmonics (with noninteger multiple of ac-side fundamental frequency) in PWM current-source drive systems, which will be elaborated in next section. Moreover, comparing the new fundamental component in PWM pattern after adding θ_{comp}, $\vec{S}_{wr1}^{\text{SHE}_1}$ in (9), with the original SHE fundamental component, $\vec{S}_{wr1}$ in (5), we can obtain that $\vec{S}_{wr1}^{\text{SHE}_1} = \vec{S}_{wr1}$. It means that the modulation index and the fundamental phase angle are not changed by θ_{comp} (the modulation index is maintained at 1 and the fundamental phase angle is still equal to the delay angle α), and therefore, θ_{comp} will not affect the dc-link current control as well as the speed control of PWM current-source drives.

In the aforementioned analysis, to investigate the realization of SHE-modulated converters' interharmonics compensation capability, we only consider the sideband harmonics introduced by the SHE fundamental component $\vec{S}_{wr1}$ and the compensation signal θ_{comp}. Similarly, the harmonic components in SHE PWM pattern will also produce the sideband harmonics after adding the compensation signal θ_{comp}. For example, the two nearest sideband harmonics, $\vec{S}_{wr\_Ls}^{\text{SHE}_h}$ and $\vec{S}_{wr\_Rs}^{\text{SHE}_h}$, with frequencies of $h\omega_{sr} \pm \omega_{\text{comp}}$ will be produced by the hth-order harmonics in SHE pattern $\vec{S}_{wrh}$ after adding θ_{comp}. They may affect the performance of interharmonics compensation and introduce other unexpected interharmonics in the system. However, on the one hand, since ω_{comp} will be noninteger multiple of ω_{sr} for interharmonics compensation, the frequencies of $\vec{S}_{wr\_Ls}^{\text{SHE}_h}$ and $\vec{S}_{wr\_Rs}^{\text{SHE}_h}$, $h\omega_{sr} \pm \omega_{\text{comp}}$, will not be equal to the frequencies of $\vec{S}_{wr\_Ls}^{\text{SHE}_1}$ and $\vec{S}_{wr\_Rs}^{\text{SHE}_1}$, $\omega_{sr} \pm \omega_{\text{comp}}$. Therefore, they will not affect the performance of interharmonics compensation. On the other hand, since the harmonic components in SHE pattern ($\vec{S}_{wrh}$) are much less significant than the fundamental component ($\vec{S}_{wr1}$), the produced sideband harmonics will be insignificant that have an ignorable influence on the system when M_{comp} is small.

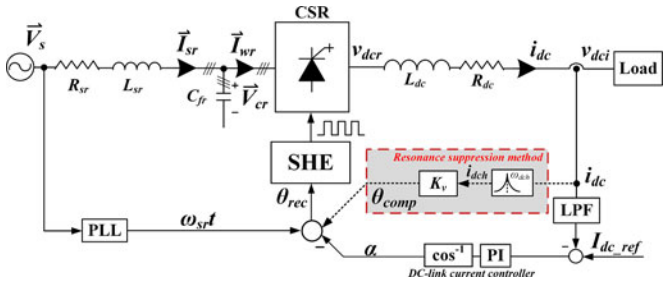

Fig. 4. Dc-link current control loop in speed control scheme shown in Fig. 3.

IV. Detailed Analysis on the Realization DC-Link Virtual Impedance

As discussed in the previous section, the compensation signal introduced into the converter's firing angle can enable the interharmonics compensation capability of SHE-modulated PWM converter by the two sideband harmonics produced in PWM pattern. In this section, to suppress the resonance caused by the harmonics interaction, the realization of dc-link virtual impedance through utilizing the two sideband harmonics will be analyzed in detail.

A. Equivalent DC-Link Virtual Impedance Introduced by the Resonance Suppression Method

According to Figs. 1 and 3, the dc-link current control loop in the speed control scheme of PWM current-source motor drives can be depicted as shown in Fig. 4. In Fig. 4, $\vec{V}_s$ is the phasor of grid voltage; $\vec{I}_{sr}$ is the phasor of grid-side line current; $\vec{I}_{wr}$ is the phasor of grid-side PWM current; $\vec{V}_{cr}$ is the phasor of grid-side capacitor voltage; v_{dcr} and v_{dci} are the rectifier-side and inverter-side dc-link voltage, respectively; R_{sr}, L_{sr}, and C_{fr} are the line resistance, line inductance, and filter capacitance in

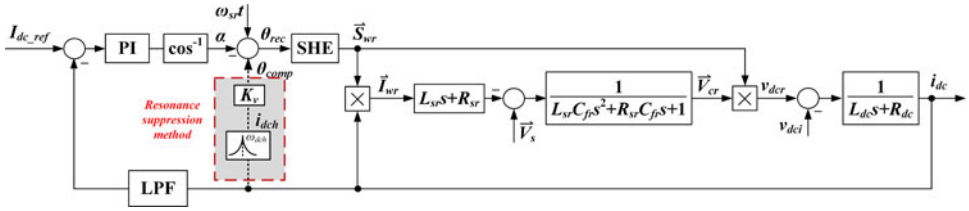

Fig. 5. Control diagram of dc-link current loop.

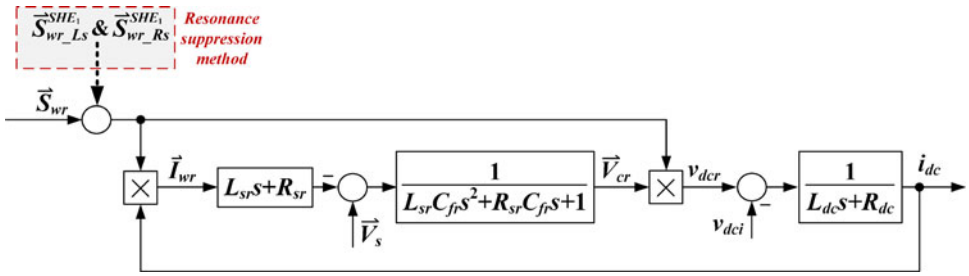

Fig. 6. Simplified diagram of dc-link current loop.

grid side, respectively; $L_{\rm dc}$ and $R_{\rm dc}$ are the dc-link inductance and resistance, respectively. In addition, we assume that the resonance due to the harmonics interaction results in significant dc-link current harmonic with ω_{dch}-frequency at steady state, defined as $i_{dch} = I_{dch}\sin(\omega_{dch}t + \varphi_{dch})$ (I_{dch} and φ_{dch} are the magnitude and phase angle, respectively). Therefore, to actively suppress the harmonics interaction through the dc link so as to avoid the resonance, the proposed dc-link virtual impedance-based resonance suppression method is required to increase the dc-link impedance at ω_{dch}-frequency as mentioned in Section II. Then, we can obtain that $\theta_{\rm comp}$ in Fig. 4 as (10). Note that K_v is a tunable complex coefficient in the proposed resonance suppression method to realize the magnitude amplification and the phase shift of i_{dch}. Since the phase shift of an ac signal is usually realized in time domain through signal delay or differential which may affect the system stability, K_v is recommended as a real coefficient in [3]. In the following analysis, we consider K_v as a real number

$$\theta_{\rm comp} = K_v I_{dch}\sin(\omega_{dch}t + \varphi_{dch}). \tag{10}$$

Based on the modulation function theory [20], [21], the relationship between the grid side and the dc link linked through the PWM process can be obtained as

$$\vec{I}_{wr} = i_{\rm dc}\vec{S}_{wr} = [i_{\rm dc}S_{wra}, i_{\rm dc}S_{wrb}, i_{\rm dc}S_{wrc}] \tag{11}$$

$$v_{dcr} = \vec{V}_{cr} \bullet \vec{S}_{wr} = v_{cra}S_{wra} + v_{crb}S_{wrb} + v_{crc}S_{wrc} \tag{12}$$

where v_{cra}, v_{crb}, and v_{crc} are the capacitor voltage of each phase. Based on (11) and (12), the control diagram of dc-link current loop shown in Fig. 4 can be described as Fig. 5.

By taking (10) into (9), we can obtain the two sideband harmonics in PWM pattern produced by the resonance suppression method at steady state as shown in (13). In addition, as discussed in the previous section, the resonance suppression method will not affect other components in PWM pattern with a small compensation signal. Then, Fig. 5 can be simplified to Fig. 6

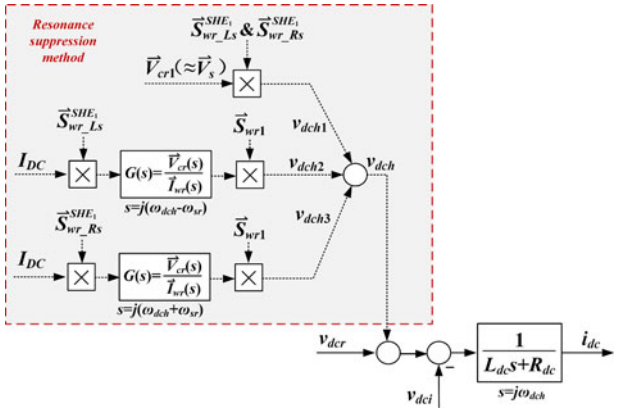

Fig. 7. Simplified diagram of dc link at ω_{dch} frequency.

$$\begin{cases} \vec{S}^{\rm SHE_1}_{wr\_Ls} \approx j0.5K_v I_{dch}e^{-j((\omega_{dch}-\omega_{sr})t+\alpha+\varphi_{dch})} \\ \vec{S}^{\rm SHE_1}_{wr\_Rs} \approx -j0.5K_v I_{dch}e^{j((\omega_{dch}+\omega_{sr})t-\alpha+\varphi_{dch})}. \end{cases} \tag{13}$$

Furthermore, based on (11)–(13), it can be obtained that the $\vec{S}^{\rm SHE_1}_{wr\_Ls}$ and $\vec{S}^{\rm SHE_1}_{wr\_Rs}$ will produce the rectifier-side dc-link voltage harmonics at ω_{dch} frequency (defined as v_{dch}) mainly through three ways (defined as $v_{dch1}, v_{dch2}, v_{dch3}$, respectively), and Fig. 6 can be further simplified to Fig. 7 at ω_{dch}. With respect to v_{dch1}, it is generated by the fundamental component in capacitor voltage, $\vec{V}_{cr1}$, and the two sideband harmonics $\vec{S}^{\rm SHE_1}_{wr\_Ls}$ and $\vec{S}^{\rm SHE_1}_{wr\_Rs}$ as shown in Fig. 7. Assuming that the grid

voltage is harmonicless and neglecting the small voltage drop on the line impedance in high-power drive systems, we can obtain that $\vec{V}_{cr1} \approx \vec{V}_s \triangleq -jV_s e^{j\omega_{sr}t}$, where V_s is the magnitude of grid voltage. Then, based on (12) and (13), it can be obtained that

$$\begin{aligned} v_{dch1} &= \vec{V}_{cr1} \bullet \vec{S}^{\mathrm{SHE}_1}_{wr\_Ls} + \vec{V}_{cr1} \bullet \vec{S}^{\mathrm{SHE}_1}_{wr\_Rs} \\ &\approx (-1.5K_v V_s \sin\alpha) I_{dch} \sin(\omega_{dch}t + \varphi_{dch}). \end{aligned} \tag{14}$$

With respect to the generation of v_{dch2} and v_{dch3}, according to (11), the dc component in dc-link current, I_{DC}, will produce two interharmonics in PWM current ($\vec{I}_{wr}$) with ($\omega_{dch} \pm \omega_{sr}$) frequencies through $\vec{S}^{\mathrm{SHE}_1}_{wr\_Ls}$ and $\vec{S}^{\mathrm{SHE}_1}_{wr\_Rs}$, respectively, at first. Then, through the grid-side circuit, the two interharmonics with ($\omega_{dch} \pm \omega_{sr}$) frequencies will be produced in the capacitor voltage ($\vec{V}_{cr}$) correspondingly. The introduced two interharmonic components in capacitor voltage generate v_{dch2} and v_{dch3} at dc link through the fundamental component in PWM pattern ($\vec{S}_{wr1}$). The grid-side circuit can be represented by the transfer function $G(s) = \vec{V}_{cr}(s) \big/ \vec{I}_{wr}(s)$ as shown in Fig. 7, and according to Fig. 6, it equals to (15) at harmonic frequencies. Based on (11)–(13), v_{dch2} and v_{dch3} can be obtained as (16) and (17), respectively

$$G(s) = \frac{\vec{V}_{cr}(s)}{\vec{I}_{wr}(s)} = \frac{L_{sr}s + R_{sr}}{L_{sr}C_{fr}s^2 + R_{sr}C_{fr}s + 1} (s \neq j\omega_{sr}) \tag{15}$$

$$\begin{aligned} v_{dch2} &= (I_{\mathrm{DC}} \vec{S}^{\mathrm{SHE}_1}_{wr\_Ls} G_-) \bullet \vec{S}_{wr1} \\ &\approx (0.75K_v I_{\mathrm{DC}} |G_-|) I_{dch} \cos(\omega_{dch}t + \varphi_{dch} + \angle G_-) \\ G_- &\triangleq G(s)\big|_{s=j(\omega_{dch}-\omega_{sr})} \end{aligned} \tag{16}$$

$$\begin{aligned} v_{dch3} &= (I_{\mathrm{DC}} \vec{S}^{\mathrm{SHE}_1}_{wr\_Rs} G_+) \bullet \vec{S}_{wr1} \\ &\approx (-0.75K_v I_{DC} |G_+|) I_{dch} \cos(\omega_{dch}t + \varphi_{dch} + \angle G_+) \\ G_+ &\triangleq G(s)\big|_{s=j(\omega_{dch}+\omega_{sr})} \end{aligned} \tag{17}$$

The division of v_{dch} by the previously defined i_{dch} ($i_{dch} = I_{dch}\sin(\omega_{dch}t + \varphi_{dch})$) can be considered as a virtual impedance Z_v introduced at dc link by the resonance suppression method as illustrated in Fig. 8. Based on (14), (16), and (17), Z_v can be obtained as (18). It can be observed from (18) that Z_v is related to the coefficient K_v in the resonance suppression method. In the following analysis, according to different resonance conditions, we will discuss the selection of K_v to enable the Z_v's attenuation effect on dc-link harmonics so as to suppress the resonance caused by the harmonics interaction

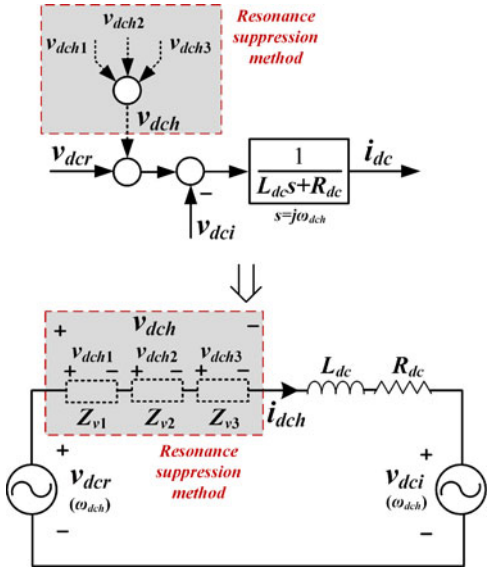

Fig. 8. Illustration of dc-link virtual impedance introduced by the resonance suppression method.

$$\frac{v_{dch}}{i_{dch}} = Z_v = Z_{v1} + Z_{v2} + Z_{v3}, \text{ where}$$

$$\begin{cases} Z_{v1} = v_{dch1}/i_{dch} = -1.5K_v V_s \sin\alpha \\ Z_{v2} = v_{dch2}/i_{dch} \\ \quad = 0.75K_v I_{DC} |G_-| \left(\cos(\angle G_-)\cot(\omega_{dch}t + \varphi_{dch}) - \sin(\angle G_-)\right) \\ Z_{v3} = v_{dch3}/i_{dch} \\ \quad = -0.75K_v I_{\mathrm{DC}} |G_+| \left(\cos(\angle G_+)\cot(\omega_{dch}t + \varphi_{dch}) - \sin(\angle G_+)\right). \end{cases} \tag{18}$$

B. Relationship Between K_v and Z_v Under Different Resonance Conditions

In [3], an estimation method of resonance conditions in high-power PWM current-source drives is proposed. It can accurately predict the motor-side fundamental frequency (steady-state inverter operating frequency) at which the resonance will be excited by the harmonics interaction, and the frequencies of the significant dc-link current harmonics caused by the resonance. Based on the information provided by the estimation method, the dc-link virtual impedance-based method realizes the attenuation on corresponding dc-link current harmonics so as to suppress the resonance caused by the harmonics interaction.

The estimation method of system resonance conditions can be briefly illustrated by Fig. 9. In Fig. 9, the horizontal axis represents the motor-side fundamental frequency (defined as ω_{si}), and the vertical axis is the frequency of dc-link harmonics. As discussed in [3], the frequencies of the dc-link current harmonics introduced by the harmonics interaction are only

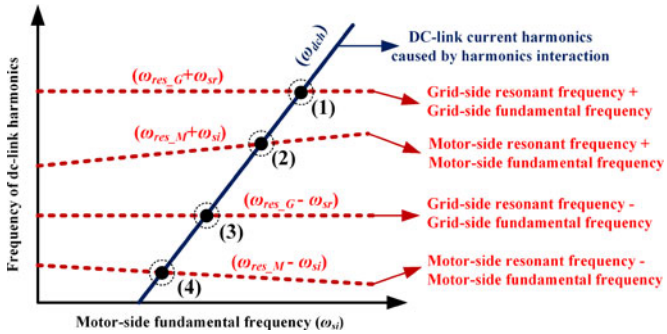

Fig. 9. Illustration of resonance conditions estimation method.

related to the PWM pattern of two converters and the motor-side fundamental frequencies. Since the SHE PWM pattern is offline designed and fixed during online implementation, the frequencies of the dc-link current harmonics (ω_{dch}) are known under different motor-side fundamental frequencies. The ω_{dch} can be represented by the solid lines, and for the convenience of explanation, only one of the lines is drawn in Fig. 9 which represents one of the dc-link current harmonics. The four dash lines in Fig. 9 represent the grid-side *LC* resonant frequency (defined as ω_{res_G}) plus/minus the grid-side fundamental frequency (ω_{sr}), and the motor-side *LC* resonant frequency (defined as ω_{res_M}) plus/minus the motor-side fundamental frequency (ω_{si}). They can be considered as the reflection of ac-side resonant frequency to dc link through PWM process, and their overlap can be guaranteed not to occur with the selected ac-side filter parameters. The system resonance will be excited when the solid line intersects with the dash line as the four intersection points shown in Fig. 9, and the corresponding motor-side fundamental frequency and the frequency of the significant dc-link current harmonic caused by the resonance can be known according to Fig. 9. To suppress the resonance, the proposed method can be enabled when the motor operates at the frequency (ω_{si}) around each intersection point, by selecting the passband frequency of the resonant filter at the corresponding ω_{dch} on the solid line during the online implementation (as shown in Fig. 4). If considering the variation and inaccuracy of system parameters, the ac-side resonant frequency (ω_{res_G} and ω_{res_M}) may change so that causes the shift of the dash lines in Fig. 9. Note that the solid line has no relationship with the system parameters so as not to be affected. As a result, the intersection points will shift along the solid line. To avoid being affected by this issue, the proposed resonance suppression method can stay active at any motor fundamental frequency (ω_{si}), which can be simply realized by assigning the resonant filter's passband frequency to be the value of the solid line (ω_{dch}) all the time. With respect to the resonance conditions shown in Fig. 9, since $\omega_{dch} = \omega_{\mathrm{res}\_G} + \omega_{sr}$ at Point (1), it means that the system resonance is excited by the $(\omega_{dch} - \omega_{sr})$-frequency interharmonics at grid side. Similarly, the Points (2), (3), and (4) represent the system resonance resulted from the $(\omega_{dch} - \omega_{si})$-frequency interharmonics at motor side, $(\omega_{dch} + \omega_{sr})$-frequency interharmonics at grid side, and $(\omega_{dch} + \omega_{si})$-frequency interharmonics at motor side, respectively. At each intersection point, the relationship between Z_v and K_v as shown in (18) can be further simplified as follows:

1) *Resonance occurs at motor side [Point (2) and Point (4)]:* Since the overlap of dash lines will not occur as mentioned previously, the resonance will not be excited at the grid side and the motor side simultaneously. Therefore, if the resonance occurs at motor side, the two frequencies of the grid-side interharmonics, $(\omega_{dch} - \omega_{sr})$ and $(\omega_{dch} + \omega_{sr})$, will be far from the grid-side resonant frequency. As a result, the $|G_-|$ and $|G_+|$ in (18) will be small, and the virtual impedance Z_v will be dominated by Z_{v1} as shown in (19)

$$Z_v \approx Z_{v1} = -1.5K_v V_s \sin\alpha. \tag{19}$$

2) *Resonance excited by the $(\omega_{dch} - \omega_{sr})$-frequency interharmonics at grid side [Point (1)]:* If the resonance occurs at grid side by the $(\omega_{dch} - \omega_{sr})$-frequency interharmonics, due to the significant amplification effect of the grid-side *LC* resonance, Z_{v2} will be dominant. Moreover, according to [22], the small dc choke in PWM current-source system will result in a certain shift up of ac-side resonant frequency so that the phase shift of the ac-side interharmonics at resonant frequency will approach positive 90°. The $\angle G_-$ in (18) can be approximately considered as 90°, and we can obtain (20) as

$$Z_v \approx Z_{v2} = -0.75K_v I_{\mathrm{DC}} |G_-|. \tag{20}$$

3) *Resonance excited by $(\omega_{dch} + \omega_{sr})$-frequency interharmonics at grid side [Point (3)]:* Similarly, if the resonance occurs at grid side by the $(\omega_{dch} + \omega_{sr})$-frequency interharmonics, we can obtain that

$$Z_v \approx Z_{v3} = +0.75K_v I_{\mathrm{DC}} |G_+|. \tag{21}$$

C. Selection of K_v to Enable Z_v's Attenuation Effect on DC-Link Current Harmonics

As mentioned previously, K_v is recommended to be a real number. It can be observed that, after choosing K_v as a negative real number in (19) and (20) and a positive real number in (21), Z_v becomes a virtually introduced resistance that can enhance the attenuation effect of dc link on current harmonics, so that realizes the active suppression of the resonance caused by the harmonics interaction.

With respect to the magnitude of K_v, it is obvious that the larger the $|K_v|$ is, the stronger resonance suppression the Z_v will perform. However, according to (10), the magnitude of the compensation signal θ_{comp} equals to $|K_v I_{dch}|$ ($M_{\mathrm{comp}} = |K_v I_{dch}|$). The large $|K_v|$ will increase M_{comp} so that the approximations based on the Bessel function's properties in Section III may be invalid, which may result in some negative impacts on the system as follows:

1) Degrade the Suppression Performance

According to the aforementioned analysis, the virtual impedance Z_v shown in (18)–(21) is derived based on the approximation of $J_1(M_{\mathrm{comp}}) \approx 0.5\, M_{\mathrm{comp}}$ in Section III. Taking Z_{v1} in (19) as an example, without this assumption, Z_{v1} will

TABLE I
PARAMETERS OF SIMULATION AND EXPERIMENTAL SYSTEM

	Simulation	Experiment
Nominal power	1.15 MVA	10 kVA
Nominal grid voltage (line-to-line)	4160 V	208 V
Frequency	60 Hz	60 Hz
Grid-side line inductance (L_{sr})	0.12 p.u.	0.15 p.u.
Grid-side filter capacitance (C_{fr})	0.43 p.u.	0.40 p.u.
Dc choke (L_{dc})	0.46 p.u.	0.58 p.u.
Motor rated voltage (line-to-line)	4000 V	208 V
Motor rated power	1100 hp	2.67 hp
Motor rated speed	1190 rpm	1720 rpm
Motor-side filter capacitance (C_{fi})	0.32 p.u.	0.20 p.u.
Motor stator leakage inductance (L_{lsi})	0.14 p.u.	0.35 p.u.
Motor stator resistance (R_{si})	0.015 p.u.	0.18 p.u.
Motor magnetizing inductance (L_m)	4.21 p.u.	4.66 p.u.
Motor rotor leakage inductance (L_{lri})	0.14 p.u.	0.35 p.u.
Motor rotor resistance (R_{ri})	0.011 p.u.	0.07 p.u.
Load torque (T_L)	3000 Nm	1.53 Nm

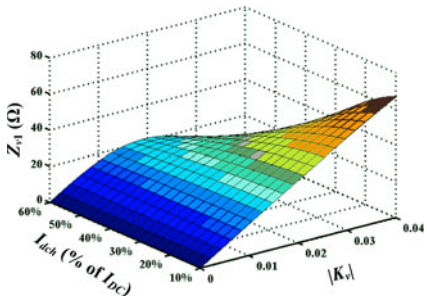

Fig. 10. Analysis of $|K_v|$'s influence on the virtual impedance based on a high-power PWM current-source drive application.

be as

$$Z_{v1} = -3J_1(K_v I_{dch}) V_s \sin\alpha / I_{dch}. \tag{22}$$

Note that polarity of K_v is selected to be negative in this case as mentioned previously. When $|K_v|$ increases, according to the property of $J_1(\cdot)$, the linear approximation will lose effectiveness gradually; and when it is further increased, the monotonicity of $J_1(\cdot)$ will be lost and the polarity may even be changed. If so, the suppression performance of Z_v will be degraded, and Z_v may even result in detrimental effect with the selected polarity of K_v. Take a real high-power PWM current-source drive application for example, the parameters of which are listed in the column "Simulation" of Table I. Fig. 10 shows the influence of $|K_v|$ and I_{dch} on Z_{v1} under the rated condition. It can be observed that, when $|K_v|$ is large, the linear relationship between Z_{v1} and $|K_v|$ as shown in (19) will lose effectiveness and Z_{v1} even drops as $|K_v|$ increases. Such problem will be aggravated when I_{dch} is larger and $|K_v|$ is further increased.

For the other two conditions, $Z_v \approx Z_{v2}$ in (20) and $Z_v \approx Z_{v3}$ in (21), since $|G_-|$ and $|G_+|$ will be significant when resonance occurs, the expected linear region between Z_v and $|K_v|$ will further shrink.

2) *Affect the Motor Speed Control*

The conclusion that $\theta_{\rm comp}$ will not affect the modulation index of PWM converter is obtained by comparing $\vec{S}_{wr1}^{\rm SHE_1}$ in (9) with $\vec{S}_{wr1}$ in (5). Such conclusion is based on the approximation of $J_0(M_{\rm comp}) \approx 1$. However, when $|K_v|$ increases, such approximation will become invalid and the $J_0(\cdot)$ will be far less than 1 with a large $|K_v|$. As a result, the modulation index will be significantly altered by $\theta_{\rm comp}$, which will affect the motor speed control. Considering the previously-mentioned drive system as an example again, the influence of $|K_v|$ and I_{dch} on CSR's modulation index (M_{sr1}) under rated condition is shown in Fig. 11. We can observe that the large $|K_v|$ will significantly deviate the modulation index from 1 (the modulation index of the SHE scheme is fixed at 1 as mentioned previously). If neglecting the system power loss, the voltage drop on grid line impedance and the system harmonics, (23) can be obtained at steady state based on the system active power balance as

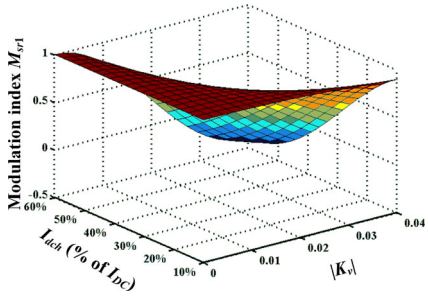

Fig. 11. Analysis of $|K_v|$'s influence on the modulation index based on a high-power PWM current-source drive application.

$$\cos\alpha = \frac{P_{\rm motor}}{1.5 V_s I_{\rm DC} M_{sr1}} \tag{23}$$

where $P_{\rm motor}$ is the active power consumption of the motor. Since the dc component of dc-link current ($I_{\rm DC}$) is controlled to track the reference $I_{\rm dc\_ref}$, which is generated by the motor drive FOC scheme as shown in Fig. 3, it has no relationship with the CSR's modulation index (M_{sr1}). As a result, according to (23), the significant deviation of M_{sr1} will greatly change the delay angle α, which will affect the dc-link current control. Furthermore, the decrease of M_{sr1} will increase the cosα at the left-hand side of (23). Since the value of cosα has an upper limit of 1, the significant deviation of M_{sr1} may even break the system active power balance as shown in (23). Therefore, the large $|K_v|$ may even result in the instability of the motor speed control after adopting the proposed suppression method.

3) *Introduce the Unexpected Interharmonics in the System*

During the analysis of SHE-modulated converters' interharmonics compensation capability enabled by the $\theta_{\rm comp}$, we only considered the two nearest sideband harmonics produced by the fundamental SHE component and the $\theta_{\rm comp}$, $\vec{S}_{wr\_Ls}^{\rm SHE_1}$ and $\vec{S}_{wr\_Rs}^{\rm SHE_1}$, and neglected other sideband harmonics in far region. This is based on the approximation of $J_k(M_{\rm comp}) \approx 0$ ($k \geq 2$). However, such approximation will also be invalid when $|K_v|$ increases, especially for the second nearest sideband harmonics. According to (8) and (10), the second nearest sideband harmonics will have the magnitude of $|J_2(K_v I_{dch})|$ and the frequencies of $(\omega_{sr} \pm 2\omega_{dch})$ with respect to the dc-link virtual

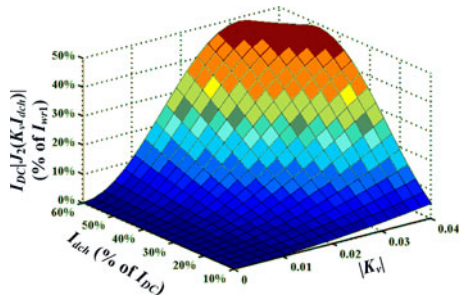

Fig. 12. Analysis of $|K_v|$'s influence on the interharmonics in grid-side PWM current based on a high-power PWM current-source drive application.

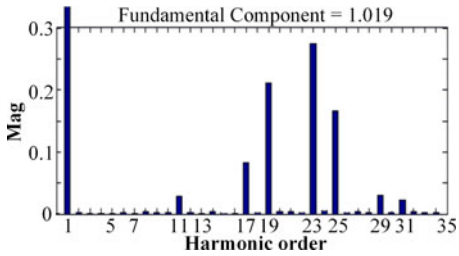

Fig. 13. Harmonics content of the adopted nine-pulse SHE PWM pattern.

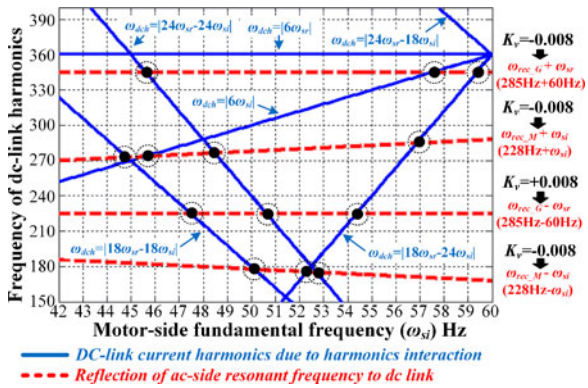

Fig. 14. Estimation of resonance conditions for the simulation system.

impedance based method. When $|K_v|$ is large, their magnitude cannot be ignored. Reacting with the dc-link current, it may introduce significant $(\omega_{sr} \pm 2\omega_{dch})$-frequency interharmonics with the magnitude of $I_{\rm DC}|J_2(K_v I_{dch})|$ in grid-side PWM current $\vec{I}_{wr}$. For the drive application mentioned previously, Fig. 12 shows the influence of $|K_v|$ and I_{dch} on the magnitude of such interharmonics (I_{wr1} in Fig. 12 is the magnitude of fundamental grid-side PWM current). It can be observed that the large $|K_v|$ will result in the significant $(\omega_{sr} \pm 2\omega_{dch})$-frequency interharmonics in grid-side PWM current. Since $\omega_{sr} \pm 2\omega_{dch}$ are comparatively low frequencies as can be observed in next section, the grid-side *LC* circuit cannot effectively attenuate such interharmonics, so that the interharmonics with the same frequencies will be introduced into the grid-side line current which will affect the grid power quality. Besides their influence on the grid side, such second nearest sideband harmonics will also react with the grid-side capacitor voltage to produce interharmonics in dc link and may further introduce interharmonics in motor side through CSI.

Moreover, other sideband harmonics in PWM pattern produced by the harmonic SHE components and the $\theta_{\rm comp}$ may also result in unexpected interharmonics in the system with a large $|K_v|$. With respect to the drive application, their situations are similar to Fig. 12.

As a result, the magnitude of K_v has to be selected with consideration of the above tradeoff.

V. Simulation Results

To verify the analysis of the dc-link virtual impedance-based resonance suppression method in this paper, the simulation is conducted on a 1.15 MVA/4160 V/60 Hz PWM current-source induction motor drive application, and the system parameters are listed in Table I. The nine-pulse SHE scheme is used in CSR, and adopted in CSI when motor operates at high fundamental frequencies. Its harmonic content is shown in Fig. 13.

The estimation of system resonance conditions with respect to the simulation system can be illustrated by Fig. 14 (the grid-side and motor-side resonant frequency, $\omega_{\rm res\_G}$ and $\omega_{\rm res\_M}$, are calculated to be 285 and 228 Hz, respectively). The explanation of Fig. 14 can refer to Fig. 9. To suppress the resonance caused by the harmonics interaction, the dc-link virtual impedance-based method is adopted around each intersection point in Fig. 14. For the coefficient K_v in the suppression method, according to the analysis in Section IV (part *B*), when the solid lines intersect with the first (uppermost), second and fourth (lowermost) dash line, K_v is selected to be a negative number; and when the solid lines intersect with the third dash line, K_v is selected to be a positive number as shown in Fig. 14. With respect to the selection of K_v's magnitude ($|K_v|$), the three aspects discussed in Section IV (part *C*) need to be considered. According to the discussion based on this simulation system as the example (see Figs. 10–12), $|K_v|$ is selected to be 0.008 in this section as shown in Fig. 14. Note that the selection of $|K_v|$ is analyzed at the rated condition of the drive system in aforementioned discussions. The appropriate range of $|K_v|$ can be extended according to the normal operation conditions.

Fig. 15 shows the simulation results of steady-state grid-side line current harmonics, dc-link current harmonics and motor-side stator current harmonics under different motor-side fundamental frequencies (without using the suppression method). It can be observed that, without attenuation of harmonics interaction, the resonance will be excited at certain motor-side fundamental frequencies and result in significant interharmonics in entire system as the high peaks shown in Fig. 15. Fig. 16 shows the simulation results of the grid-side line current, dc-link current and motor-side stator current after adopting the proposed suppression method with the selection of K_v. Comparing Fig. 16 to Fig. 15, we can observe that the dc-link virtual impedance concept is effectively realized by the proposed resonance suppression method at all resonance conditions and any motor speeds, as the high peaks in Fig. 15 are greatly attenuated in Fig. 16. It verifies the analysis in this paper.

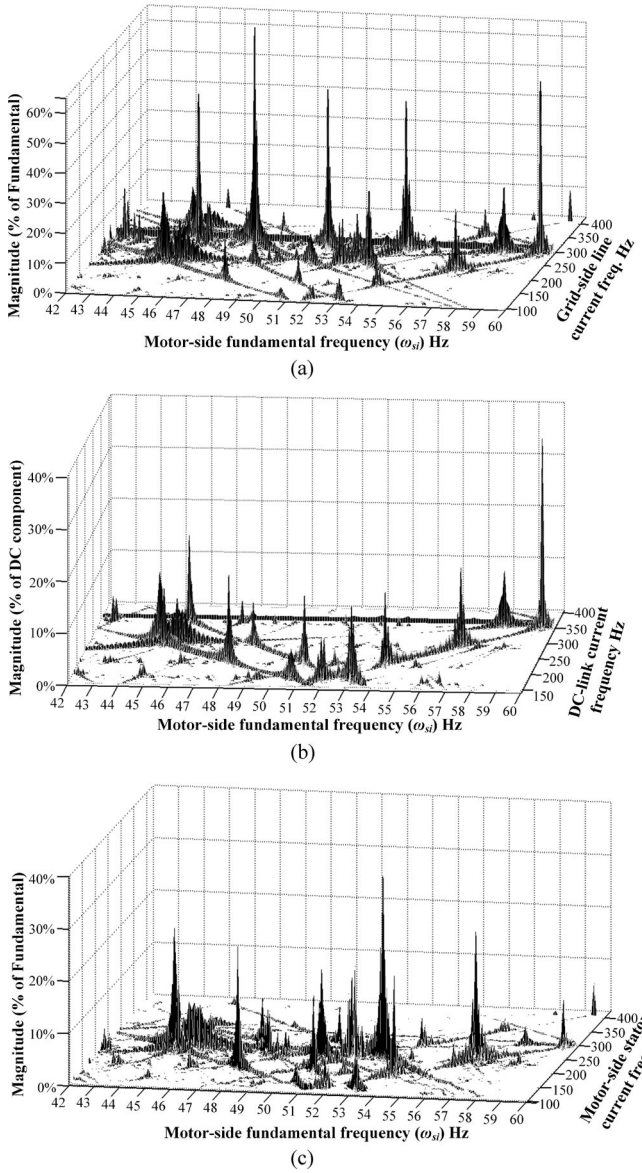

Fig. 15. System current harmonics before using the resonance suppression method [3].

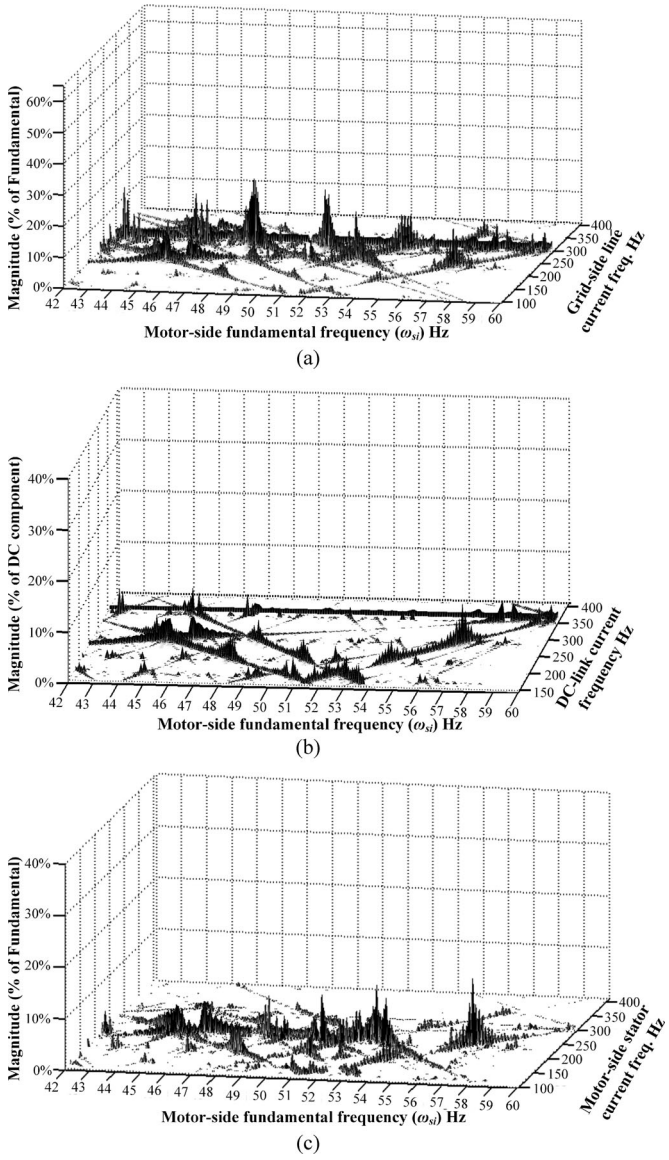

Fig. 16. System current harmonics after using the resonance suppression method.

VI. Experimental Results

To further verify the validity of the analysis, plenty of real-time experiments have been carried out on a 10 kVA/208 V/60 Hz PWM current-source induction motor drive prototype. The parameters of the experimental system are listed in Table I, and the same nine-pulse SHE pattern as in the simulation section (see Fig. 13) is used for both the CSR and the CSI. To save space, one example of resonance suppression at 53-Hz motor-side fundamental frequency is provided.

The estimation of system resonance conditions in respect to the experimental system can be drawn as shown in Fig. 17 (ω_{res_G} and ω_{res_M} are calculated to be 261 and 209 Hz, respectively, based on the parameters of experimental system). According to Fig. 17, when motor fundamental frequency is at 53 Hz, the two dc-link current harmonics with 318 and 192 Hz

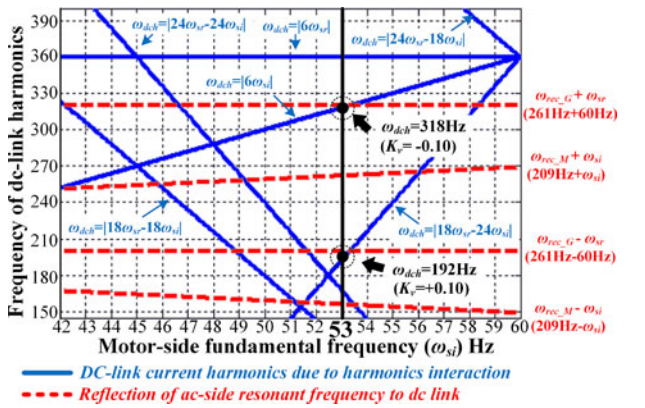

Fig. 17. Estimation of resonance conditions for the experimental system.

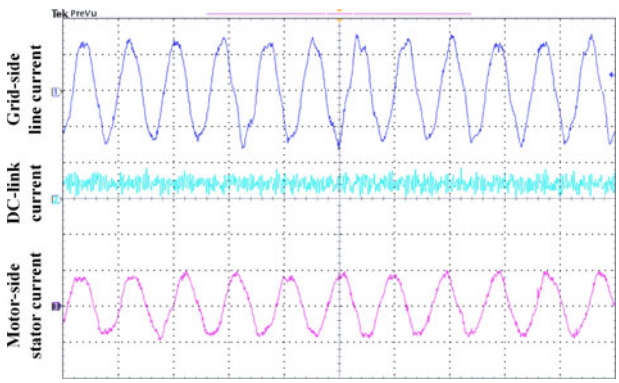

Fig. 18. Waveforms of system current at $\omega_{si} = 53$ Hz before using suppression method (10 A/div., 20 ms/div.).

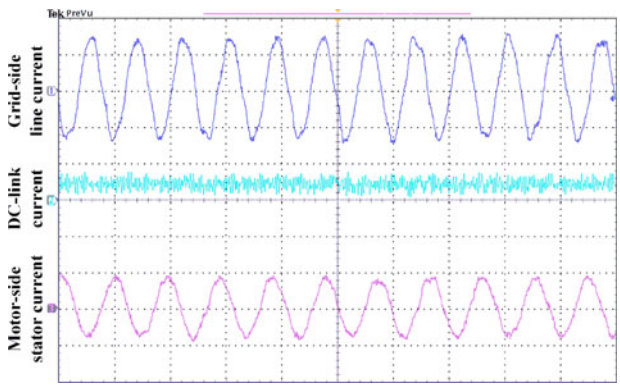

Fig. 20. Waveforms of system current at $\omega_{si} = 53$ Hz after using suppression method (10 A/div., 20 ms/div.).

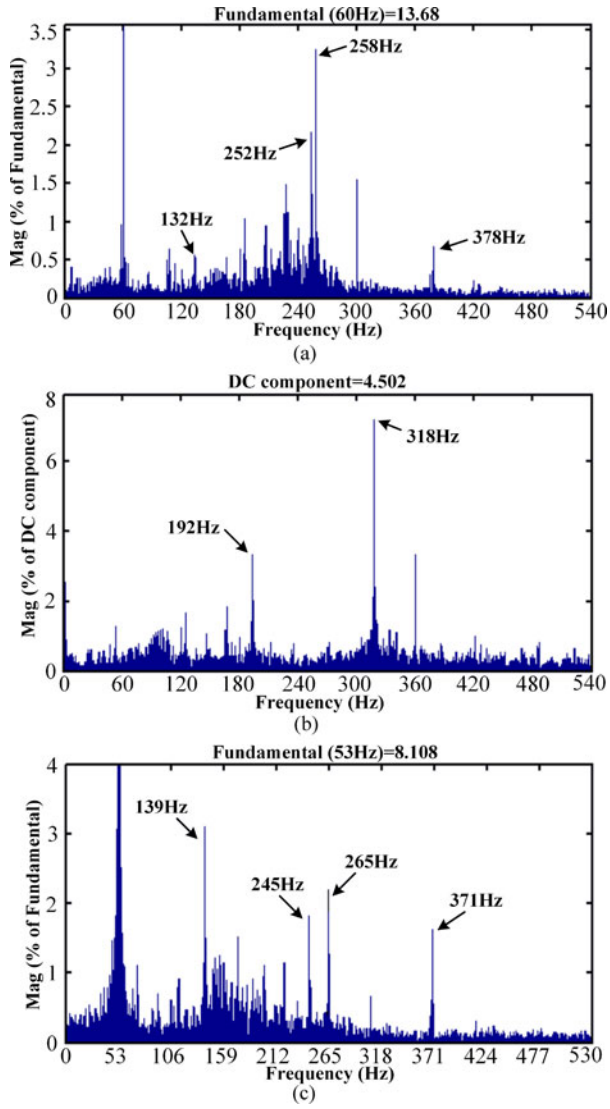

Fig. 19. FFT analysis of system currents at $\omega_{si} = 53$ Hz before using suppression method.

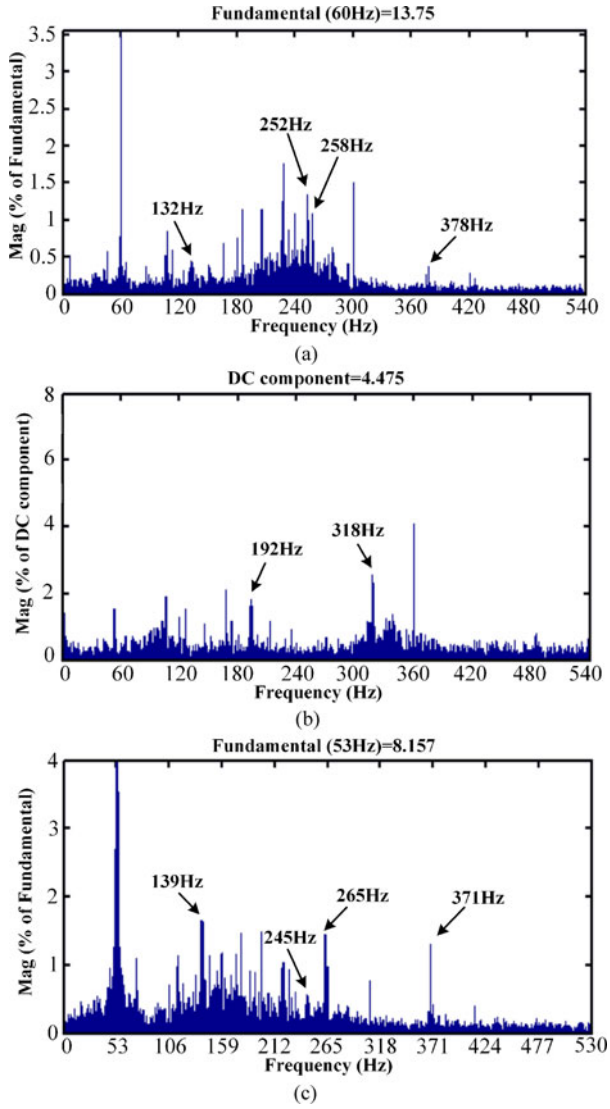

Fig. 21. FFT analysis of system currents at $\omega_{si} = 53$ Hz after using suppression method.

TABLE II
MAGNITUDE OF HARMONICS BEFORE AND AFTER SUPPRESSION

	Before Suppression		After Suppression	
Grid-side line current (% of fundamental)	Fundamental = 13.68 A		Fundamental = 13.75 A	
	252 Hz	258 Hz	252 Hz	258 Hz
	2.18%	3.27%	1.20%	1.01%
Dc-link current (% of dc component)	Dc component = 4.502 A		Dc component = 4.475 A	
	192 Hz	318 Hz	192 Hz	318 Hz
	3.68%	7.30%	1.89%	2.12%
Motor-side stator current (% of fundamental)	Fundamental = 8.108 A		Fundamental = 8.157 A	
	139 Hz	245 Hz	139 Hz	245 Hz
	3.12%	1.88%	1.60%	0.45%
	265 Hz	371 Hz	265 Hz	371 Hz
	2.11%	1.66%	1.45%	1.33%

are close to the first dash line and the third dash line, respectively, which will be greatly amplified by the system resonance. To suppress these harmonics, the proposed resonance suppression method is required to virtually increase the dc-link impedance at both the 318 and 192 Hz ($\theta_{\rm comp}$ includes two components with 318 and 192 Hz, respectively, which can be realized by two sets of K_v and resonant filter as shown in Fig. 3). Following the same procedure of K_v's selection for the simulation system in Section V, we select $K_v = -0.1$ for the 318 Hz component and $K_v = +0.1$ for the 192 Hz component, respectively, with respect to the experimental system.

Figs. 18 and 19 show the waveforms and FFT analysis of the steady-state grid-side line current, dc-link current and motor-side stator current at 53-Hz motor-side fundamental frequency before using the suppression method. It can be observed that significant 318 and 192 Hz harmonics are contained in dc-link current as shown in Fig. 19(b). In addition, through the fundamental component in CSR's modulation function (60 Hz) and the fundamental component in CSI's modulation function (53 Hz), the corresponding 258 Hz (= 318 Hz – 60 Hz) and 252 Hz (= 192 Hz + 60 Hz) interharmonics are significant in grid-side line current as shown in Fig. 19(a), and 371 Hz (= 318 Hz + 53 Hz), 265 Hz (= 318 Hz – 53 Hz), 245 Hz (= 192 Hz + 53 Hz) and 139 Hz (= 192 Hz – 53 Hz) interharmonics are significant in motor-side stator current as shown in Fig. 19(c). Since the 378 Hz (= 318 Hz + 60 Hz) and 132 Hz (= 192 Hz – 60 Hz) interharmonics are far from the grid-side resonant frequency, they are not obvious in grid side. After adopting the proposed suppression method with the selection of K_v, the waveforms and FFT analysis of the system currents are shown in Figs. 20 and 21, respectively. The magnitude of those harmonics before and after using the suppression method is summarized in Table II according to the FFT analysis in Figs. 19 and 21. We can observe that the proposed method significantly mitigates the dc-link current harmonics so that attenuates the harmonics interaction phenomenon in PWM current-source drive system, which can be observed from the greatly attenuated interharmonics at both the grid side and the motor side.

VII. CONCLUSION

In this paper, an in-depth study of the dc-link virtual impedance-based resonance suppression method is presented. The mechanism of the interharmonics compensation capability of SHE-modulated PWM current-source converters enabled by the dc-link virtual impedance-based method is thoroughly investigated. Based on the investigation, more detailed analysis is provided on the realization of the dc-link virtual impedance. In addition, in order to enhance the attenuation effect of dc link on the harmonics interaction, the selection of coefficient in the suppression method is also discussed according to different resonance conditions in high-power PWM current-source drive systems. Simulation and experimental results demonstrate that, with the coefficient selected by following the analysis in this paper, the dc-link virtual impedance-based method can effectively increase the attenuation effect of dc link on current harmonics so that reduces the harmonics interaction in PWM current-source drives through the dc link, and therefore, suppress the resonance resulted from the harmonics interaction.

REFERENCES

[1] B. Wu, *High-Power Converters and AC Drives*. New York, NY, USA: Wiley, 2006, pp. 189–191.

[2] Y. W. Li, M. Pande, N. R. Zargari, and B. Wu, "DC-link current minimization for high-power current-source motor drives," *IEEE Trans. Power Electron.*, vol. 24, no. 1, pp. 232–240, Jan. 2009.

[3] Y. Zhang and Y. W. Li, "Investigation and suppression of harmonics interaction in high-power PWM current-source motor drives," *IEEE Trans. Power Electron.*, vol. 30, no. 2, pp. 668–679, Feb. 2015.

[4] J.C. Wiseman and B. Wu, "Active damping control of a high-power PWM current source rectifier for line-current THD reduction," *IEEE Trans. Ind. Electron.*, vol. 52, no. 3, pp. 758–764, Jun. 2005.

[5] F. Liu, B. Wu, N. R. Zargari, and M. Pande, "An active damping method using inductor-current feedback control for high-power PWM current-source rectifier," *IEEE Trans. Power Electron.*, vol. 26, no. 9, pp. 2580–2587, Sep. 2011.

[6] M. H. Bierhoff and F. W. Fuchs, "Active damping for three-phase PWM rectifiers with high-order line-side filters," *IEEE Trans. Ind. Electron.*, vol. 56, no. 2, pp. 371–379, Feb. 2009.

[7] J. D. Ma, B. Wu, N. R. Zargari, and S. C. Rizzo, "A space vector modulated CSI-based AC drive for multimotor applications," *IEEE Trans. Power Electron.*, vol. 16, no. 4, pp. 535–544, Jul. 2001.

[8] Y. Sato and T. Kataoka, "A current-type PWM rectifier with active damping function," *IEEE Trans. Ind. Appl.*, vol. 32, no. 3, pp. 533–541, May 1996.

[9] Z. Wang, B. Wu, D. Xu, and N. R. Zargari, "Dynamic capacitor voltage control of high power current source converter fed PMSM drives for LC resonance suppression," in *Proc. IEEE Int. Symp. Ind. Electron.*, 2010, pp. 792–797.

[10] S. A. S. Grogan, D. G. Holms, and B. P. McGrath, "High performance voltage regulation of current source inverters," *IEEE Trans. Power Electron.*, vol. 26, no. 9, pp. 2439–2448, Sep. 2011.

[11] J. Dannehl, F. W. Fuchs, S. Hansen, and P. Bach, "Investigation of active damping approaches for PI-based current control of grid-connected pulse width modulation converters with LCL filters," *IEEE Trans. Ind. Appl.*, vol. 46, no. 4, pp. 1509–1517, Jul. 2010.

[12] Y. W. Li, "Control and resonance damping of voltage-source and current-source converters with LC filters," *IEEE Trans. Ind. Electron.*, vol. 56, no. 5, pp. 1511–1521, May 2009.

[13] H. Zhou, Y. W. Li, N. R. Zargari, Z. Cheng, R. Ni, and Y. Zhang, "Selective harmonic compensation (SHC) PWM for grid-interfacing high-power converters," *IEEE Trans. Power Electron.*, vol. 29, no. 3, pp. 1118–1127, Mar. 2014.

[14] R. Ni, Y. W. Li, Y. Zhang, N. R. Zargari, and G. Cheng, "Vitrual impedance based selective harmonic compensation (VI-SHC) PWM for current source rectifier," *IEEE Trans. Power Electron.*, vol. 29, no. 7, pp. 3346–3356, Jul. 2014.

[15] A. M. Qiu, Y. W. Li, B. Wu, D. Xu, N. R. Zargari, and Y. Liu, "High performance current-source inverter fed induction motor drive with minimal harmonic distortion," in *Proc. IEEE Power Electron. Spec. Conf.*, 2007, pp. 79–85.
[16] Y. W. Li, M. Pande, N. R. Zargari, and B. Wu, "An input power factor control strategy for high-power current-source induction motor drive with active front-end," *IEEE Trans. Power Electron.*, vol. 25, no. 2, pp. 352–359, Feb. 2010.
[17] Y. W. Li, M. Pande, N. R. Zargari, and B. Wu, "Power-factor compensation for PWM CSR-CSI-fed high-power drive system using flux adjustment," *IEEE Trans. Power Electron.*, vol. 24, no. 12, pp. 3014–3019, Dec. 2009.
[18] Z. Wang, B. Wu, D. Xu, and N. R. Zargari, "Hybrid PWM for high-power current-source-inverter-fed drives with low switching frequency," *IEEE Trans. Power Electron.*, vol. 26, no. 6, pp. 1754–1763, Jun. 2011.
[19] D. G. Holmes and T. A. Lipo, *Pulse Width Modulation for Power Converters Principles and Practice*. New York, NY, USA: IEEE Press, 2003, pp. 409–411.
[20] L. Hu and R. Yacamini, "Harmonic transfer through converters and HVDC links," *IEEE Trans. Power Electron.*, vol. 7, no. 3, pp. 514–525, Jul. 1992.
[21] D. Zhang, W. Xu, and Y. Liu, "On the phase sequence characteristics of interharmonics," *IEEE Trans. Power Del.*, vol. 20, no. 4, pp. 2563–2569, Oct. 2005.
[22] H. Zhou, Y. W. Li, N. R. Zargari, and Z. Y. Cheng, "Input resonance investigation and LC filter design for PWM current source rectifiers," in *Proc. IEEE Energy Convers. Congr. Expo.*, 2010, pp. 2079–2086.

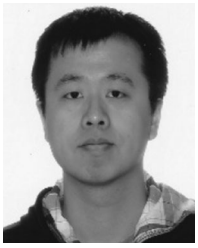

Ye Zhang (S'13) received the B.Eng. and M.Sc. degrees in electrical engineering from Beihang University, Beijing, China, in 2008 and 2011, respectively. He is currently working toward the Ph.D. degree in electrical power engineering at the Department of Electrical and Computer Engineering, University of Alberta, Edmonton, AB, Canada.

His current research interests include current-source converters, ac motor drives, and control system design.

Yun Wei Li (S'04–M'05–SM'11) received the B.Sc. degree in electrical engineering from Tianjin University, Tianjin, China, in 2002, and the Ph.D. degree from Nanyang Technological University, Singapore, in 2006.

In 2005, he was a Visiting Scholar with Aalborg University, Aalborg, Denmark. From 2006 to 2007, he was a Postdoctoral Research Fellow at Ryerson University, Toronto, ON, Canada. In 2007, he worked at Rockwell Automation Canada and later joined the Department of Electrical and Computer Engineering, University of Alberta, Edmonton, AB, Canada, in the same year. His research interests include distributed generation, microgrid, renewable energy, high power converters, and electric motor drives.

Dr. Li is currently an Associate Professor at the University of Alberta. He serves as an Associate Editor for IEEE TRANSACTIONS ON POWER ELECTRONICS and IEEE TRANSACTIONS ON INDUSTRIAL ELECTRONICS. He received the 2013 Richard M. Bass Outstanding Young Power Electronics Engineer Award from IEEE Power Electronics Society.